Supplementary Information

Impacts of Localized Charge Accumulation on Photocurrent Dynamics in Metal-MoS_2 Contacts

Deogkyu Choi[1,†], Seungho Bang[1,†], Juchan Lee[1,†], Chaewon Lee[1], Jieun Jo[1], Young Joo Yu[1], Chan Kwon[1], Hayoung Ko[2], Ki Kang Kim[2], Jinho Ahn[3,], Eun Kyu Kim[1,*], and Mun Seok Jeong[1,4,*]*

[1]Department of Physics, Hanyang University, Seoul 04763, Republic of Korea

[2]Department of Energy Science, Sungkyunkwan University, Suwon 16419, Republic of Korea

[3]Division of Materials Science and Engineering, Hanyang University, Seoul 04763, Republic of Korea

[4]Department of Semiconductor Engineering, Hanyang University, Seoul 04763, Republic of Korea

* Address correspondence to mjeong@hanyang.ac.kr (Mun Seok Jeong), jiahn@hanyang.ac.kr (Jinho Ahn), and ek-kim@hanyang.ac.kr (Eun Kyu Kim)

† These authors contributed equally.

1L-MoS_2-based FETs fabrication process.

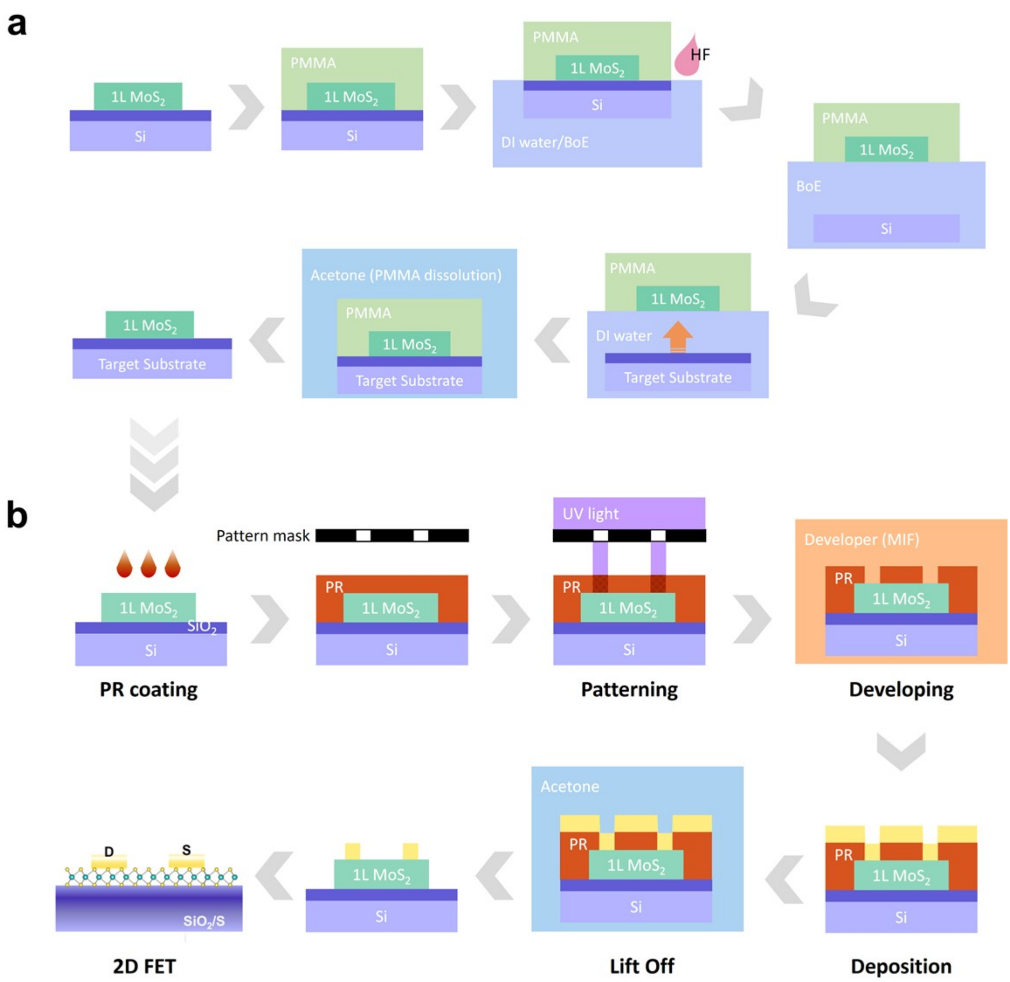

Figure S1. (a) Conventional wet transfer process with PMMA and HF acid. (b) Patterning and metallization for Ti/Au electrodes.

The chemical vapor deposition as-grown MoS_2 sample was spin-coated with PMMA and floated onto deionized (DI) water. HF acid was poured into DI water, and then PMMA-MoS_2 sample was detached from the Si-SiO_2 substrate. It was subsequently rinsed several times in DI water for neutralization and transferred to a target substrate. After drying with DI water for 24 h, PMMA was dissolved, and a 1L-MoS_2 sample was prepared. Metallization is required to fabricate the FET. For that, the photoresist was spin-coated onto the transferred sample and pre-baked at 120 ˚C (1~2 minutes). The photoresist was then patterned by UV light using a lithography pattern generator (Litho maskless, Standard Science) and developed using the MIF solution. Using sputtering or thermal evaporation, Ti/Au (5/50 nm) electrodes for the drain/source contact were deposited on the 1L-MoS_2 sample and rinsed with acetone to remove the photoresist residue. After metallization, thermal annealing (200 ℃, 1~2 hours) was conducted to ensure the ideal device performance.

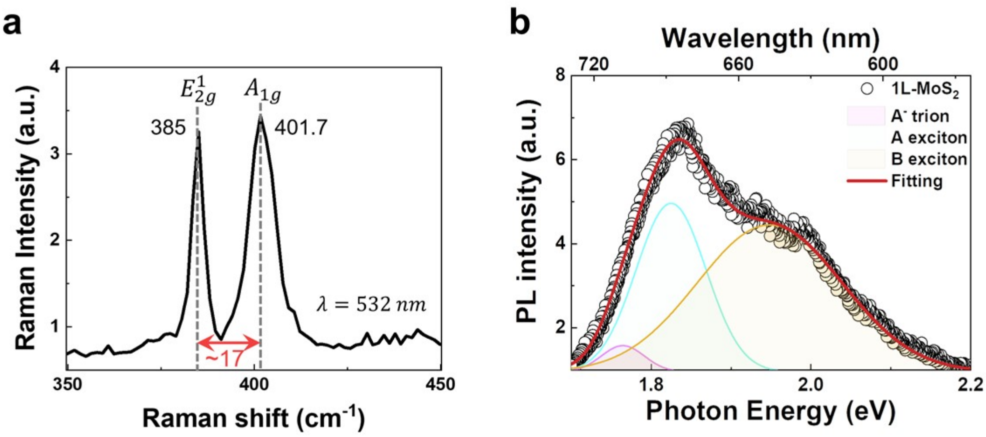

Figure S2. (a) Raman and (b) PL spectrum of 1L-MoS_2 measured with 532 nm laser.

Evaluation of the electrical properties with IV curves

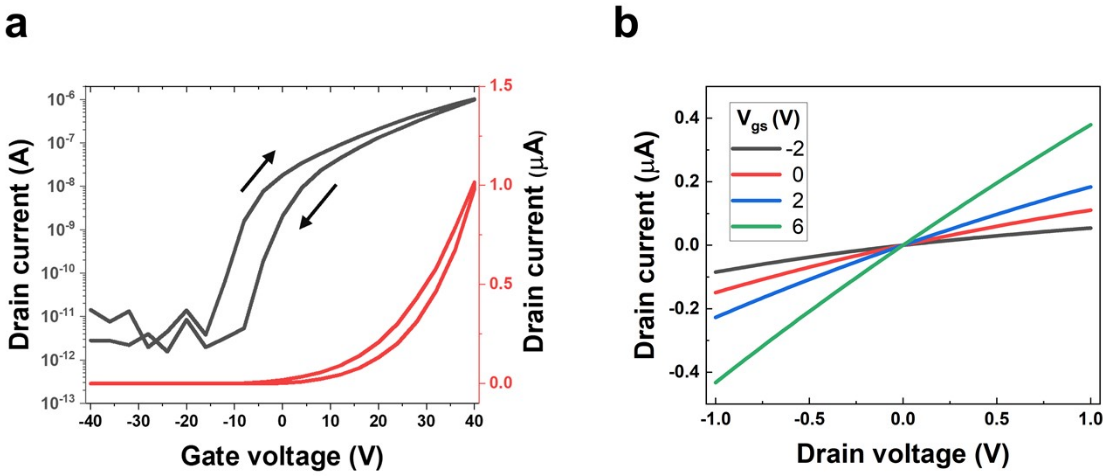

Figure S3. (a) Transfer characteristics measured at V_{ds} = 1 V and (b) output characteristics of the MoS_2 device varied with V_{gs}.

The transfer and output characteristics were determined to confirm the electrical properties of the fabricated 1L-MoS_2 device and to determine its effectiveness. In Figure S3a, the hysteresis observed in dual-sweeping transfer curves indicates the presence of interfacial trap states between MoS_2 and SiO_2. Device field-effect mobility (μ_{eff}) and subthreshold swing (SS) can be obtained by fitting the transfer characteristics. The channel length, width, and oxide thickness of the device were L = 12.1 μm, W = 30.2 μm, and d = 300 nm, respectively. With each ε_0 and ε_r corresponding to the vacuum permittivity and the gate oxide relative permittivity, $C_{ox} = \varepsilon_0\varepsilon_r / d$ = 11.5 nF/cm^2. The device mobility was estimated using the equation of field-effect mobility:

$$\mu_{eff} = \frac{L}{W}\frac{dI_{ds}/dV_{gs}}{C_{ox}V_{ds}}$$

thus, μ_{eff} = 1.94 cm^2/V·s and the subthreshold swing is obtained as:

$$SS = \left(\frac{d\log_{10} I_{ds}}{dV_{gs}}\right)^{-1}$$

Therefore, SS = 2.8 V/dec on the transfer curve. As shown in Figure S3b, Ohmic contact behavior is well defined by the tendency of the drain current to vary with the drain voltage (output characteristics).

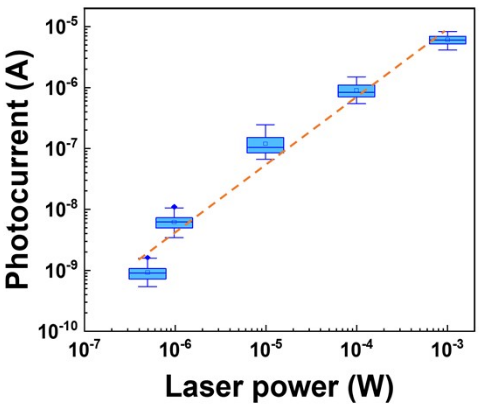

Figure S4. Linear relation between the localized PC and laser power and their linear fitting line in the CA region (orange line).

Schottky barrier height calculation by 2D thermionic emission

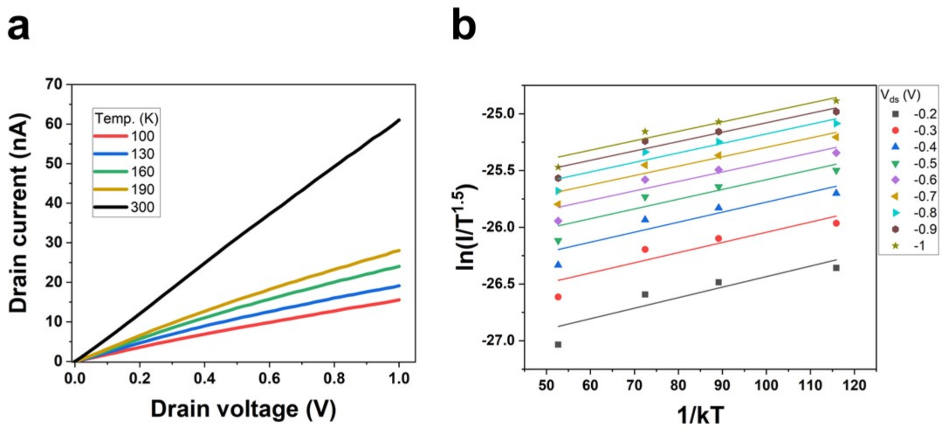

Figure S5. (a) the output characteristics under the various temperatures. (b) the Arrhenius plot under V_{ds} from 0.2 to 1 V.

To ensure SBH behavior in the MS junction, the drain to source I-V was investigated under different temperatures using a 2D thermionic theory:

$$I_{ds} = AA_{2D}^{*}T^{3/2}exp[-\frac{q}{kT}(\Phi_B - \frac{V_{ds}}{n})] \tag{S1}$$

where A is the contact area, $A_{2D}^{*}= (q\sqrt{8\pi k^3 m^*})/h^2$ is the effective Richardson constant, q is the elementary charge, $m^* = 0.42m_0$ is the effective mass of electron in 1 L-MoS_2, Φ_B is SBH, and n is the ideality factor. In contrast to 3D bulk semiconductors, this 2D model accounts for the reduced dimensionality of monolayer MoS_2, including the $T^{1.5}$ dependency, reflecting the 2D carrier distribution in its conduction band. To confirm that the MS junction band bending forms the CA region, Figure S5 shows that the SBH is calculated using the 2D thermionic emission equation from S1 by plotting the temperature-dependent output curves to the Arrhenius plot ($\ln(I/T^{1.5})$ against 1/kT). The slope was obtained from this plot and subsequently expressed as slope versus V_{ds}. In Figure S5c, the y-intercept indicates -$q\Phi_B$, that is, SBH is found to be -10 meV. This result demonstrates that ohmic contact and CA region formation are valid in the Ti/Au-contacted 1L-MoS_2 device. As a result, band bending at the MS junction is shallow, and the LCA region forms dominated by any potential barrier effects. In essence, these findings confirm that the negative SBH is the primary cause of photocurrent reduction, indicating the presence of activated trap states and excess carriers in the LCA regio, resulting in enhanced scattering.

Arrhenius plot with hysteresis charge and N_t calculation with temperature dependent transfer curves.

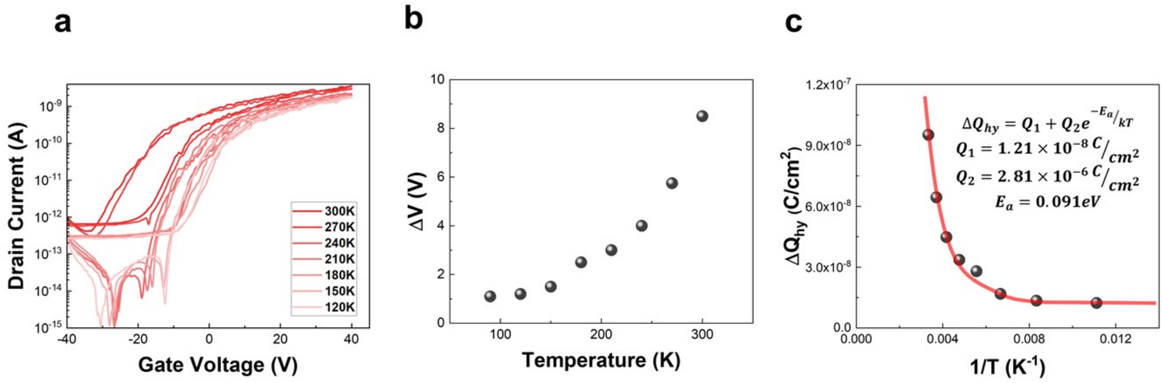

Figure S6. (a) Dual-sweeping transfer characteristics with temperature modulation from 120 to 300 K. (b) The threshold voltage difference depending on temperature. (c) Arrhenius plot fitted by the exponential hysteresis charge equation of the hysteresis charge with simple exponential components and thermal activation energy.

The temperature-dependent transfer curves provide hysteresis behavior widening the hysteresis window as increasing temperature, as shown in Figure S6a. Further, threshold voltage difference (ΔV) between forward and backward sweep curves can be obtained in Figure S6b and evaluated as a hysteresis charge. This total hysteresis charge (ΔQ_{hy}) is fitted by the exponential model with fixed and mobile trap charges:

$$\Delta Q_{hy} = Q_1 + Q_2 e^{-E_a/kT} \qquad \text{(S2)}$$

where E_a is thermal activation energy. In Figure S6c, Q_1 and Q_2 are evaluated as 1.21×10^{-8} C/cm^2 and 2.81×10^{-6} C/cm^2 indicating the fixed and mobile charges by thermal activation within the interface region in general. Further, thermal activation energy is obtained with 0.091 eV, indicating trap level mainly occurring the interfacial capturing and releasing trap process. The interface trap density N_t is also calculated with 5.94×10^{11} cm^{-2} in the 300 K temperature region, using the formula $N_t = \Delta Q_{hy}/q$."

Repeated observation of the localized PC reduction in other samples.

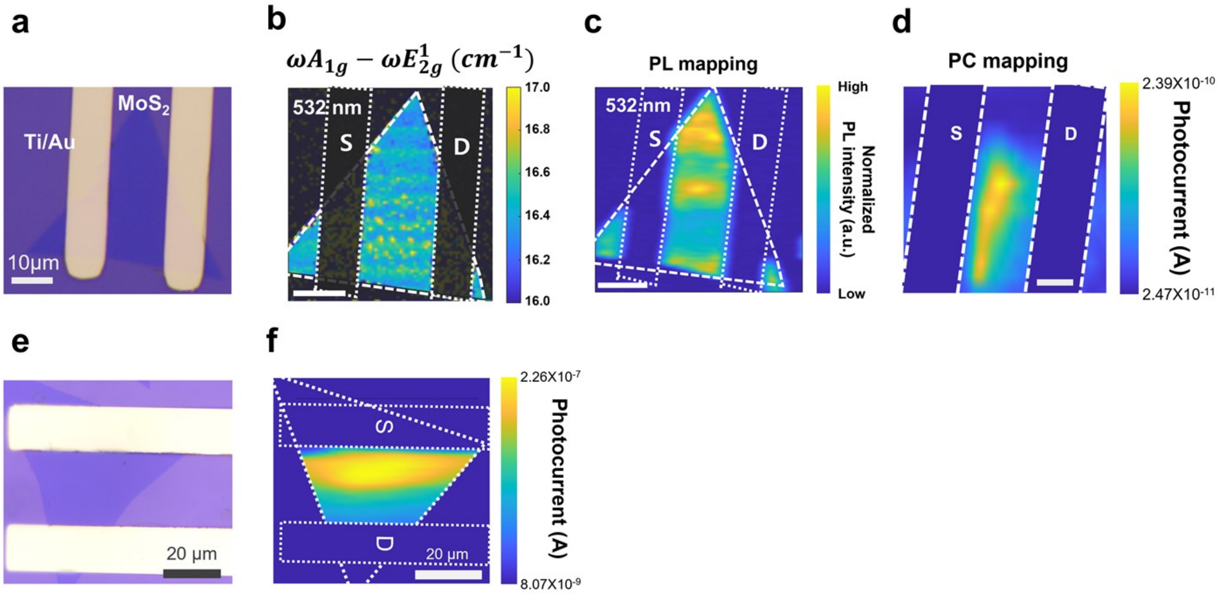

Figure S7. (a) OM, (b) Raman shift difference between A_{1g} and E^1_{2g} mapping, (c) PL mapping, and (d) PCM images of other sputter-fabricated Ti/Au-contacted 1L-MoS_2-based FET under V_{ds} = 0.5 V and 500 nW of 532 nm laser (white solid line indicates 10 μm). (e) OM, and (f) PCM images of the thermal evaporation-fabricated Ti/Au-MoS_2-based FETs.

PC degradation induced by the CA region was also observed in other devices by measuring the localized PCM. This local photocurrent reduction can occur repeatedly in 1 L-MoS_2-based optoelectronic devices because 2D materials are significantly restricted by the contact materials.

The ratio of PC intensity and width between CA and channel regions varied with drain voltage.

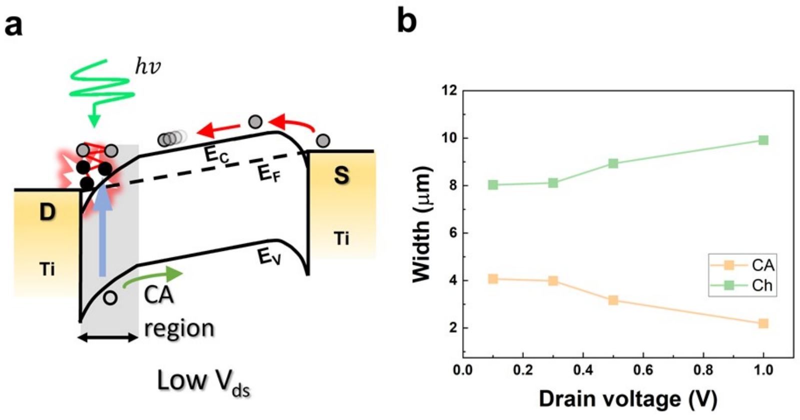

Figure S8. (a) Schematic band structures of low drain bias. (b) Width of CA and channel region comparison varied with drain voltage 0.1 to 1.0 V.

In total channel length L=12.1 μm, CA and channel region width is divided by the drain voltage. At high V_{ds}, the CA width decreased compared to the widening channel width because the forward-biased V_{ds} affected the bandwidth. In this result, the CA region induced by the MS junction can be modulated by the drain bias, and subsequently, its width decreases in the forwarding high V_{ds}.

The relationship between drain current and gate voltage.

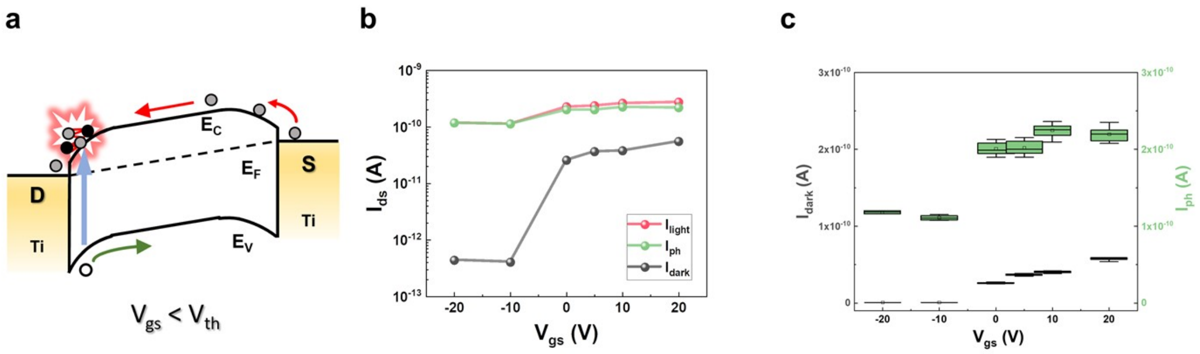

Figure S9. (a) Schematic band structures of gate bias less than threshold voltage. (b) Drain current measured at gate voltage from -20 to 20 V (red, green, and dark show the light, photo, and dark current, respectively). (c) IQR analysis of the dark and photocurrent with the same gate voltage range.

The dispersion of the position-dependent PC was reduced by increasing V_{gs}. 1L-MoS_2, a conventional n-type semiconductor, exhibits a highly conductive channel in the high positive gate voltage region. Consequently, this conductive channel significantly decreases the photocurrent generation in the entire 1L-MoS_2 channel owing to its extremely thin channel depth, which is modulated entirely by the gate voltage. Lee et al. reported that the metal-insulator transition caused by the gate voltage degrades the photocurrent generation in the 1L-MoS_2 FET. As shown in Figure S8b, c, the dark current (drain current without any illumination) consistently increased above V_{gs} = 0 V, whereas the photocurrent slightly increased at approximately V_{gs} = 0 V and decreased at high V_{gs}. This result indicates that the metal-insulator transition occurs in our 1L-MoS_2 FET, and the CA region induces a localized metallic state in the junction, resulting in localized PC reduction.

Dark and light carrier concentration depending on V_{gs} and δn extraction

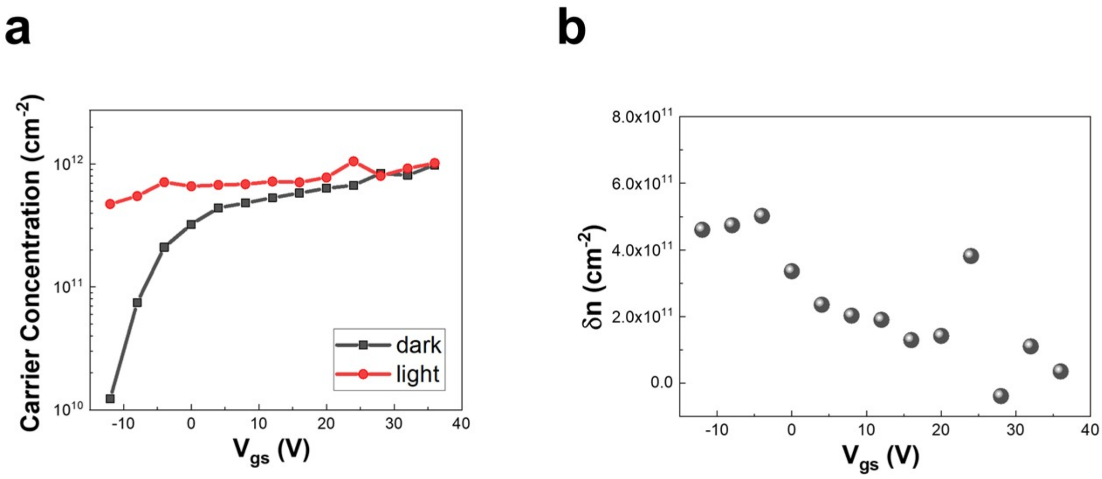

Figure S10. (a) Each carrier concentration with V_{gs} = -12 to 36 V in the case of dark and light illumination. (b) photo-excited excess carrier concentration extracted by the difference between light and dark carrier concentration.

Figure S10 illustrates the variation in channel carrier concentration as V_{gs} is swept from -12 V to 36 V under both dark and light-illuminated conditions, also the resulting excess carrier concentration generated by photoexcitation. These observations, however, represent channel-averaged carrier concentrations; further spatially-resolved measurements would help clarify the precise local effects responsible for the photocurrent reduction in the LCA region. As shown in Figure S10a, under dark conditions, the carrier concentration monotonically increases with increasing V_{gs}. In contrast, it remains consistently higher overall in the light-case. Notably, the generation of additional photo-induced carriers becomes more prominent at negative and low positive gate voltages, significantly enhancing the device's conductivity in the subthreshold region. Meanwhile, Figure S10b demonstrates that the photoexcited excess carrier concentration decreases as V_{gs} becomes more positive. This trend can be attributed to the rapidly growing intrinsic carrier density at higher V_{gs}, which reduces the relative contribution of photoexcited carriers. Overall, analysis of the extracted carrier concentrations indicates that the intrinsic carrier density and the photoexcited excess carrier density are on a similar order of magnitude, suggesting that electrons in this n-type device may play a direct role in the observed reduction of photocurrent.

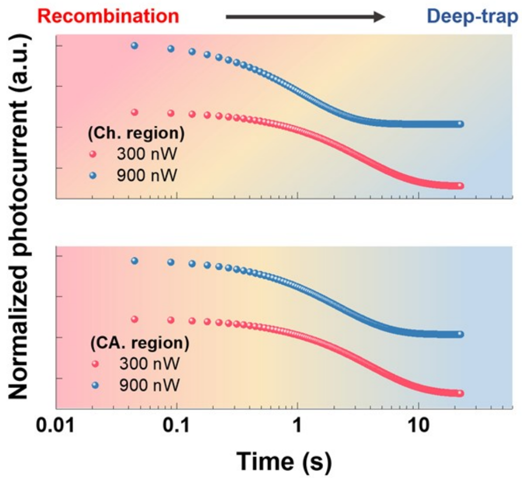

Figure S11. Normalized decaying photocurrent in both LCA and channel regions (the gradation of the background colors indicates the changing pattern from recombination centers to deep-level traps).

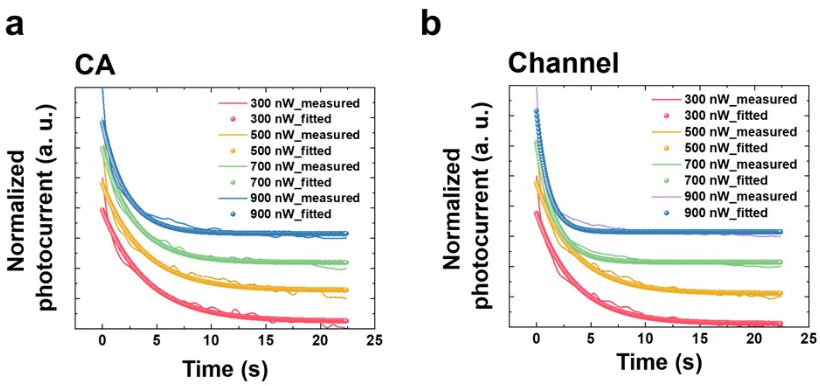

Figure S12. Normalized decaying photocurrent of (a) CA, (b) Ch regions.